ISA Transactions 176 (2026) 81–93

Contents lists available at ScienceDirect

ISA Transactions

journal homepage: www.elsevier.com/locate/isatra

Research article

Koopman-based H_∞/GH_2 control for in-wheel motor driven semi-active suspensions with magnetorheological dampers

Jie Guo [a,b], Shuyou Yu [a,b,*], Chao Ma [b]

[a] The National Key Laboratory of Automotive Chassis Integration and Bionics, Jilin University, Changchun 130025, China

[b] Department of Control Science and Engineering, Jilin University, Changchun 130025, China

HIGHLIGHTS

- A Koopman-based integrated modeling and control framework is proposed for MR semi-active suspensions.
- MR damper dynamics are globally linearized using Koopman operator theory.
- A static output feedback H_∞/GH_2 controller balances comfort, safety, and suspension stroke.
- Simulations verify improved vertical dynamics over PASOF-H_∞/GH_2 and Sky-hook control.

ARTICLE INFO

Keywords:
Electric vehicles
Semi-active suspension
Magnetorheological damper
In-wheel motor
H_∞/Generalized H_2 control

ABSTRACT

To comprehensively improve the vertical dynamics of in-wheel motor driven electric vehicles (IWM-EVs), the optimal control of semi-active suspension systems equipped with magnetorheological (MR) dampers is investigated in this paper. The conflicting objectives of ride comfort, driving safety, and suspension stroke are addressed, along with the control challenges introduced by the nonlinear behavior of the MR damper. To accommodate the strong nonlinear coupling between the MR damper and suspension system states, an integrated modeling and control framework is proposed. This framework overcomes the approximation limitations of conventional hierarchical control in handling nonlinear dissipation constraints and eliminates the discontinuities associated with fixed switching logic in segmented control architectures. However, the nonlinear coupled dynamics significantly increase the complexity of controller design and computation. In response to this issue, the Koopman operator theory is employed to derive a globally linear representation of the MR damper dynamics, upon which an integrated linear equivalent model is constructed. Furthermore, an output-feedback H_∞/Generalized H_2 (H_∞/GH_2) control strategy is developed on this basis to optimize the overall vertical performance of the vehicle. Simulation comparisons show that, relative to hierarchical control methods and the conventional Sky-hook control, the proposed integrated strategy better exploits the real-time adjustability of the MR damper, leading to notable improvements in vehicle vertical dynamics under various road excitations.

1. Introduction

Electric vehicles (EVs) are widely recognized as an eco-friendly automotive technology that contributes to sustainable transportation, owing to their lower dependence on fossil fuels and the consequent attenuation of CO_2 emissions associated with global warming [1]. In EVs, the conventional internal combustion engine is substituted with electric motors [2]. For IWM-EVs in particular, each wheel is powered by an individually controlled electric motor integrated directly into the wheel assembly. This configuration eliminates the need for conventional transmission components, leading to a more efficient and simplified drivetrain [3]. However, the integration of IWM inevitably raises the unsprung mass, which amplifies vertical vibration and compromises ride comfort [4]. Furthermore, excessive unsprung mass intensifies the inertial effects of the unsprung components, making it difficult for the tire to maintain consistent contact with the road surface under dynamic inputs [5]. These adverse effects make it more challenging to balance ride comfort, driving safety, and suspension stroke limits [6]. To address these issues, Bridgestone has developed a dynamic damping

* Corresponding author at: The National Key Laboratory of Automotive Chassis Integration and Bionics, Jilin University, Changchun 130025, China.
Email addresses: jieguo20@mails.jlu.edu.cn (J. Guo), shuyou@jlu.edu.cn (S. Yu), machao24@mails.jlu.edu.cn (C. Ma).

https://doi.org/10.1016/j.isatra.2026.06.004
Received 19 December 2025; Received in revised form 2 June 2026; Accepted 2 June 2026
Available online 9 June 2026
0019-0578/

mechanism that decouples the motor from the wheel by means of a dedicated vibration absorption system [7]. Moreover, the topology optimization of IWM is often constrained by limited wheel space and mechanical design limitations. Consequently, further improvements in vertical vibration performance for IWM-EVs are increasingly dependent on advanced control strategy design.

Numerous control strategies, including frequency-limited H_∞ control [8], fuzzy H_∞ control [9], model predictive control [10], event-triggered control [11,12], and other control methods [13,14], have been developed for active suspension systems in IWM-EVs. In contrast, research on semi-active suspension control remains relatively limited. Relative to active systems, semi-active suspensions offer advantages such as lower cost, reduced weight, and lower maintenance requirements, leading to a more favorable cost-performance trade-off [15]. Consequently, semi-active suspensions equipped with MR dampers have attracted considerable research interest. However, the inherent energy-dissipative characteristic of such systems presents fundamental challenges for controller design [16,17].

Traditional semi-active suspension strategies, such as Sky-hook [18], Ground-hook [19], and hybrid control [20], typically regulate the damping coefficient based on switching logic to comply with energy-dissipative principles. However, these methods suffer from performance degradation due to frequent switching. To further enhance system performance, a hierarchical control structure is commonly adopted [21], wherein the upper layer generates the desired damping force and the lower layer utilizes an inverse-model-based controller for precise force tracking. Nevertheless, the dissipative nonlinear constraints inherent to MR dampers present a critical challenge that must be systematically addressed in the design of the upper-layer controller [22]. For example, LQR is employed in [23] to improve the ride comfort of the vehicle. To handle parameter uncertainties and road excitations, sliding mode control is introduced [24,25]. Additionally, model predictive control strategies incorporating preview information are proposed in [26,27] to enhance vehicle dynamic performance. Although these methods respect the physical constraints of MR dampers, they inherently sacrifice optimality by operating within a 'clipped-optimal control' framework-where the theoretical control outputs are clipped to comply with damper limitations, inevitably leading to performance degradation [28]. Therefore, systematically addressing the dissipative constraint of MR dampers in controller design has become a critical issue to improve suspension performance. To this end, various methods have been proposed to explicitly account for these nonlinear dissipative constraints. For instance, a piecewise affine H_∞ controller is developed in [29], which utilizes piecewise linearization to approximate the dissipative nonlinear behavior. In [30], the nonlinear constraints are transformed via mixed logical dynamical modeling into a mixed-integer quadratic programming formulation. Although these approaches are capable of accommodating constraints, they inherently rely on piecewise or switching logic, often resulting in discontinuous transitions and compromised performance under varying operating conditions.

Subsequently, a nonlinear MPC strategy is introduced in [31] for integrated current optimization, employing parallel parameterization and GPU acceleration to enhance real-time computational efficiency. Meanwhile, an adaptive neuro-fuzzy system is applied in [32] for MR damper modeling, followed by a T-S fuzzy controller designed for real-time current regulation. However, the design of such fuzzy controllers relies substantially on expert knowledge, and their effectiveness is constrained by the precision of the predefined membership functions. In [33], a model-free reinforcement learning approach is adopted to learn control policies directly from data; nevertheless, obtaining sufficient high-quality training data remains a significant practical challenge.

Therefore, existing control strategies for MR semi-active suspension systems exhibit significant limitations in multi-objective optimization. First, present methods inadequately address the inherent dissipative nonlinearity of MR dampers, which restricts vehicle dynamic performance and impedes systematic trade-offs among ride comfort, driving safety, and suspension stroke. Second, the computational complexity associated with high-fidelity nonlinear models limits real-time implementation on resource-constrained embedded vehicle platforms. Furthermore, data-driven intelligent control methods often depend extensively on expert knowledge and high-quality training data, which limits their practical applicability.

To address these challenges, an integrated control method based on the Koopman operator for IWM driven MR semi-active suspension systems is proposed in this paper. The proposed control framework systematically addresses the multi-objective control problem for strongly nonlinear suspension systems, enabling full utilization of the dynamic potential of MR dampers to simultaneously optimize ride comfort while rigorously satisfying hard constraints. It overcomes the approximation limitations inherent in conventional hierarchical control when handling nonlinear dissipation constraints, and eliminates the discontinuities associated with fixed switching logic in segmented control architectures. Specifically, an RNN model is first developed to characterize the nonlinear dynamics of the MR damper. Additionally, an equivalent linear model of the damper is established via the Koopman operator, which accurately captures its dynamic characteristics. Subsequently, an integrated linear model of the suspension-actuator system is formulated. Based on this integrated model, a static output feedback H_∞/GH_2 controller is designed for the MR semi-active suspension. The controller employs an H_∞ norm-based approach to optimize ride comfort, while the GH_2 norm directly enforces hard constraints on driving safety, suspension stroke, and actuator saturation. Notably, the controller gains are computed offline, thereby eliminating real-time computational burden. Simulation results demonstrate that, compared with both the piecewise affine static output feedback H_∞/GH_2 (PASOF-H_∞/GH_2) and Sky-hook control methods, the proposed strategy yields enhanced overall vehicle performance under various road excitations.

2. Model description and problem statement

An integrated nonlinear model of a semi-active suspension system equipped with an MR damper in an IWM-EV is presented, which accurately captures the coupled dynamics between the damper and the suspension structure. Although this model provides a more comprehensive characterization of the system dynamics, the strong nonlinearity introduces substantial challenges for controller design, making it difficult to accommodate within conventional control methods.

2.1. Quarter-vehicle model

Based on the IWM driven system proposed by Bridgestone in [7], Fig. 1presents the quarter-vehicle vertical dynamics model incorporating a semi-active suspension.

The terms m_s, m_u, and m_d denote the sprung mass, unsprung mass, and the mass of the IWM, respectively. k_s and k_d represent the spring stiffness coefficients, while the tire is represented as a linear spring of stiffness k_t. The damping coefficients of the suspension and the motor are denoted by c_s and c_d, respectively. The vertical displacements of m_s, m_u, and m_d are respectively indicated by x_s, x_u and x_d, while x_r stands for the road excitation input. The damping force produced by the MR damper is expressed as $F(t)$. All relevant parameters and their numerical values are summarized in Table 1.

The system dynamics shown in Fig. 1can be expressed as:

$$
\begin{aligned}
& m_s\ddot{x}_s(t) + k_s\left(x_s(t) - x_u(t)\right) + c_s\left(\dot{x}_s(t) - \dot{x}_u(t)\right) = F(t) \\
& m_u\ddot{x}_u(t) + k_t\left(x_u(t) - x_r(t)\right) - k_s\left(x_s(t) - x_u(t)\right) - c_s\left(\dot{x}_s(t) - \dot{x}_u(t)\right) \\
& - k_d\left(x_d(t) - x_u(t)\right) - c_d\left(\dot{x}_d(t) - \dot{x}_u(t)\right) = -F(t)
\end{aligned}
$$

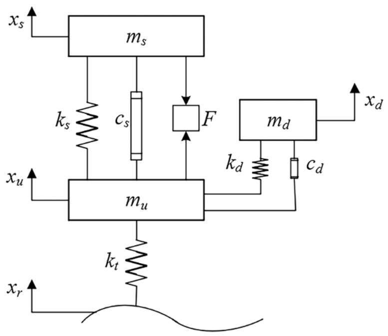

Fig. 1. IWM driven semi-active suspension model [11].

Table 1
Parameter numerical values of the suspension.

Description	Symbol	Value
Sprung mass	m_s	320 kg
Unsprung mass	m_u	40 kg
Motor mass	m_d	20 kg
Suspension stiffness	k_s	18,000 N/m
Suspension damping	c_s	1000 Ns/m
Tire stiffness	k_t	200,000 N/m
Suspension motor stiffness	k_d	15,000 N/m
Suspension motor damping	c_d	1000 Ns/m

$$m_d\ddot{x}_d(t) + k_d\left(x_d(t) - x_u(t)\right) + c_d\left(\dot{x}_d(t) - \dot{x}_u(t)\right) = 0 \tag{1}$$

For convenience, the following state vector is introduced:

$$\begin{aligned}\chi(t) &= \begin{bmatrix} x_s(t)-x_u(t) & \dot{x}_s(t) & x_u(t)-x_r(t) & \dot{x}_u(t) & x_d(t)-x_u(t) & \dot{x}_d(t)\end{bmatrix}^{\mathrm{T}} \\ &= \begin{bmatrix}\chi_1(t) & \chi_2(t) & \chi_3(t) & \chi_4(t) & \chi_5(t) & \chi_6(t)\end{bmatrix}^{\mathrm{T}}\end{aligned} \tag{2}$$

where $\chi_1(t)$ and $\chi_3(t)$ represent the suspension stroke and tire deformation, respectively; $\chi_2(t)$ and $\chi_4(t)$ denote the velocities of the sprung and unsprung masses; while $\chi_5(t)$ and $\chi_6(t)$ correspond to the displacement and velocity of the IWM. The state-space equation for system (1) is established:

$$\dot{\chi}(t) = A\chi(t) + B_1F(t) + B_2w(t) \tag{3}$$

where

$$A = \begin{bmatrix} 0 & 1 & 0 & -1 & 0 & 0 \\ -\frac{k_s}{m_s} & -\frac{c_s}{m_s} & 0 & \frac{c_s}{m_s} & 0 & 0 \\ 0 & 0 & 0 & 1 & 0 & 0 \\ \frac{k_s}{m_u} & \frac{c_s}{m_u} & -\frac{k_t}{m_u} & -\frac{c_s+c_d}{m_u} & \frac{k_d}{m_u} & \frac{c_d}{m_u} \\ 0 & 0 & 0 & -1 & 0 & 1 \\ 0 & 0 & 0 & \frac{c_d}{m_d} & -\frac{k_d}{m_d} & -\frac{c_d}{m_d}\end{bmatrix},$$

$$B_1 = \begin{bmatrix} 0 & \frac{1}{m_s} & 0 & -\frac{1}{m_u} & 0 & 0\end{bmatrix}^{\mathrm{T}}, B_2 = \begin{bmatrix} 0 & 0 & -1 & 0 & 0 & 0\end{bmatrix}^{\mathrm{T}}$$

Taking a sampling time of 0.02s, the discrete-time state-space equation for system (3) is established using the Z-transform method:

$$\chi(k+1) = G\chi(k) + H_1F(k) + H_2w(k) \tag{4}$$

where G, H_1, H_2 are the system matrices of the discrete-time model, with the same dimensions as A, B_1, B_2 in (3), respectively.

2.2. MR damper modeling

For precise modeling of the nonlinear characteristics of the MR damper, a data-driven approach based on a Recurrent Neural Network (RNN) is employed. The data and training method follow our previous work [34]. The network topology is illustrated in Fig. 2.

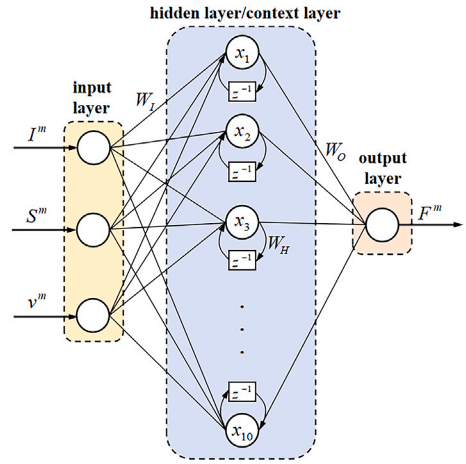

Fig. 2. Structure of the RNN model for the MR damper.

The inputs to the neural network consist of the current I^m, piston displacement S^m, piston velocity v^m, and the time-delayed outputs of the hidden layer neurons. The network output is the predicted damping force F^m. Additionally, the weight matrices W_I, W_H, and W_O represent the connections between the layers of the RNN and are used to capture the input–output relationship of the MR damper.

The state-space equation for the above RNN model is described as:

$$\begin{aligned} x^m(k+1) &= \tanh\left(W_I \times u^m(k) + W_H \times x^m(k)\right) \\ F^m(k+1) &= W_O \times x^m(k+1)\end{aligned} \tag{5}$$

where

$$x^m(k) = \begin{bmatrix} x_1^m(k) & x_2^m(k) & \dots & x_{10}^m(k)\end{bmatrix}^{\mathrm{T}}$$

represents the output of the RNN hidden layer at time k without physical meaning. The control input of the MR damper is denoted as

$$u^m(k) = \begin{bmatrix} I^m(k) & \chi_1^m(k) & \chi_2^m(k) - \chi_4^m(k)\end{bmatrix}^{\mathrm{T}} \tag{6}$$

Remark 1. As the MR damper is installed between the sprung and unsprung masses, its piston displacement provides a direct measure of the suspension stroke. The piston velocity, correspondingly, represents the relative velocity.

2.3. Nonlinear model of IWM driven semi-active suspensions with MR dampers

Based on Eqs. (4) and (5), an integrated model of the IWM driven semi-active suspension system is established, in which the damping force generated by the MR damper and the suspension control input form a pair of action–reaction forces. It should be noted that the input and output data in the neural network model Eq. (5) are normalized, whereas the variables in the suspension system Eq. (4) are physical values. Therefore, data transformation between the two domains is necessary. The normalization and denormalization operations are defined as follows:

$$r_{\text{norm}} = -1 + \frac{\left(r - r_{\min}\right)\cdot 2}{r_{\max} - r_{\min}} \tag{7}$$

$$r = \frac{\left(r_{\text{norm}} + 1\right)\left(r_{\max} - r_{\min}\right)}{2} + r_{\min} \tag{8}$$

Combining Eqs. (4)–(8) yields the complete nonlinear model of the IWM driven semi-active suspension with an MR damper, expressed as:

$$\begin{cases} \chi(k+1) = G\chi(k) + H_1\left[-\xi \cdot W_O \cdot x^m(k+1) - b\right] + H_2 w(k) \\ x^m(k+1) = \tanh\left(W_I \cdot u^m(k) + W_H \cdot x^m(k)\right) \end{cases} \tag{9}$$

where

$$\xi = \frac{F_{\max} - F_{\min}}{2}, \quad b = \frac{F_{\max} + F_{\min}}{2} \tag{10}$$

Remark 2. For the input vector $u^m(k)$ of the MR damper, the piston velocity is represented by the normalized value of $\dot{x}_s(k) - \dot{x}_u(k)$, and the piston displacement is represented by the normalized value of $x_s(k) - x_u(k)$. Therefore, for the system described in (3), the actual control input is the current $I(k)$, which is obtained by denormalizing the network output $I^m(k)$.

3. Controller design

The control problem is defined as the multi-objective optimization of the nonlinear system described in (9), subject to specified state constraints. To reduce computational complexity and improve design feasibility, firstly, an equivalent linear model of the IWM driven MR semi-active suspension system is constructed using the Koopman operator. By retaining the essential nonlinear dynamics, this model enables the complex nonlinear optimization problem to be reformulated and solved within a linear framework [35]. On this basis, a static output-feedback H_∞/GH_2 controller is developed to effectively attenuate the vertical vibration induced by road excitations. Specifically, an H_∞ norm-based optimization approach is adopted to improve ride comfort, while the GH_2 norm framework is employed to directly enforce hard constraints on driving safety, suspension stroke, and actuator saturation. The control structure is shown in Fig. 3.

3.1. Control objectives

The control objectives of the suspension system are summarized as follows [36]:

(i) Ride comfort: minimize the vertical acceleration of the sprung mass $\ddot{x}_s$ to enhance ride comfort.

(ii) Driving safety: the dynamic tire load should not exceed the static load in order to maintain driving safety.

$$k_t(x_u - x_r) < (m_s + m_u + m_d)g$$

(iii) Suspension stroke: due to mechanical design limitations, the suspension stroke is constrained by the allowable maximum value.

$$|x_s - x_u| < S_{max}$$

(iv) Actuator limitations: $I \in [0, 1]$A.

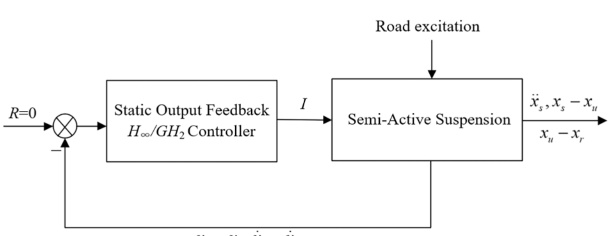

Fig. 3. Integrated control structure of the IWM driven semi-active suspension system.

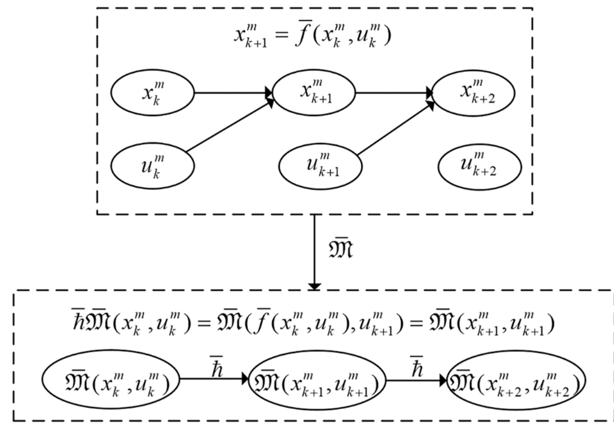

Fig. 4. Koopman operator for controlled systems.

3.2. Koopman-based linear model of IWM driven semi-active suspensions with MR dampers

The Koopman operator is introduced to linearize the RNN model of the MR damper, mapping the complex nonlinear system into a higher-dimensional linear space while preserving the nonlinear dynamics. This approach substantially reduces the complexity of both controller design and the solution of the optimization problem.

(1) The Koopman operator framework and spectral decomposition methods

The nonlinear model of the MR damper in Eq. (5) is characterized by:

$$x_{k+1}^m = \bar{f}\left(x_k^m, u_k^m\right) \tag{11}$$

where $x_k^m \in \Upsilon \subseteq \mathbb{R}^n$ denotes the output of the RNN hidden layer at time k, $u_k^m \in \mathrm{u} \subseteq \mathbb{R}^m$ is the control input, and the function $\bar{f}$ represents the state transition mapping between two consecutive time steps.

Define $\bar{\hbar}$ as the Koopman operator for the RNN model of the MR damper, and $\overline{\mathfrak{M}}$ as the observable function. As illustrated in the schematic of the Koopman operator evolution in Fig. 4, this operator maps the state evolution of the original nonlinear system onto a linear evolution in a high-dimensional space [37]. This mapping leads to the transformation of the nonlinear dynamics described by Eq. (5) into the following form:

$$\bar{\hbar}\overline{\mathfrak{M}}\left(x_k^m, u_k^m\right) = \overline{\mathfrak{M}}\left(x_{k+1}^m, u_{k+1}^m\right) = \overline{\mathfrak{M}}\left(\bar{f}\left(x_k^m, u_k^m\right), u_{k+1}^m\right) \tag{12}$$

For nonlinear systems, the observable function $\overline{\mathfrak{M}}$ is often chosen as eigenfunctions of the associated Koopman operator. Its evolution can then be characterized by the Koopman spectrum, thereby reconstructing the dynamics of the original nonlinear system as a superposition of linear models. Specifically, spectral decomposition extracts the eigenvalues and eigenfunctions of the Koopman operator, and the global dynamics are decomposed into a superposition of independent modes.

If ξ_i is an eigenfunction of the Koopman operator $\bar{\hbar}$ with eigenvalue λ_i, then:

$$\bar{\hbar}\xi_i\left(x_k^m, u_k^m\right) = \xi_i\left(\bar{f}\left(x_k^m, u_k^m\right), u_{k+1}^m\right) = \lambda_i\xi_i\left(x_k^m, u_k^m\right) \tag{13}$$

where $i = 1, 2, \ldots, N$.

Remark 3. For notational simplicity, the time step variable k in discrete-time systems is uniformly expressed in subscript form throughout this subsection.

(2) Koopman-based linear model for MR dampers

The EDMD algorithm in [38] is employed to construct a finite-dimensional approximation of the infinite-dimensional operator $\bar{h}$. The details are as follows:

Firstly, the sequences of the system states, control input, and output of the RNN model in Eq. (5) are collected to construct the following data matrices:

$$\chi_1 = \begin{bmatrix} x_1^m & \cdots & x_{k_{\max}}^m \end{bmatrix}, \chi_2 = \begin{bmatrix} x_2^m & \cdots & x_{k_{\max}+1}^m \end{bmatrix},$$

$$Y = \begin{bmatrix} F_1^m & \cdots & F_{k_{\max}}^m \end{bmatrix}, U = \begin{bmatrix} u_1^m & \cdots & u_{k_{\max}}^m \end{bmatrix}$$

where the state matrices $\chi_1 \in \mathbb{R}^{n^* k_{\max}}$ and $\chi_2 \in \mathbb{R}^{n^* k_{\max}}$, output matrix $Y \in \mathbb{R}^{q^* k_{\max}}$, input matrix $U \in \mathbb{R}^{m^* k_{\max}}$, and $k_{\max}$ is the length of the sequence.

The observable function on a finite-dimensional space ψ is defined as follows:

$$\psi\left(x_k^m\right) = \begin{bmatrix} \psi_1\left(x_k^m\right) & \psi_2\left(x_k^m\right) & \cdots & \psi_N\left(x_k^m\right) \end{bmatrix}^{\mathrm{T}} \tag{14}$$

where N is the dimensionality.

For the precise tracking of the states and output damping force of the RNN model, the following objective functions are formulated as:

$$\underset{A_{MR},B_{MR}}{\text{minimize}} \sum_{k=1}^{k_{\max}} \left\| \psi\left(x_{k+1}^m\right) - A_{MR}\psi\left(x_k^m\right) - B_{MR}u_k^m \right\|_2^2 \tag{15}$$

$$\text{minimize} \sum_{k=1}^{k_{\max}} \left\| F_k^m - C_{MR}\psi\left(x_k^m\right) \right\|_2^2 \tag{16}$$

Then, the state matrix A_{MR} and the input matrix B_{MR} of the linear system can be obtained.

Finally, the nonlinear system (9) can be reformulated in a linear framework through the following Koopman-based model:

$$\begin{cases} z_{k+1} = A_{MR} \cdot z_k + B_{MR} \cdot u_k^m \\ F_{MR_k} = C_{MR} \cdot z_k \end{cases} \tag{17}$$

where $z_k = \begin{bmatrix} \psi_1\left(x_k^m\right) & \psi_2\left(x_k^m\right) & \cdots & \psi_N\left(x_k^m\right) \end{bmatrix}^{\mathrm{T}}$ denotes the state vector of the high-dimensional linear model. $\psi_1\left(x_k^m\right)$ is taken as the output of the system, i.e., $C_{MR} = [1, 0, \ldots, 0]_{1*N}$. The terms $\psi_2\left(x_k^m\right) \ldots \psi_{11}\left(x_k^m\right)$ are the outputs of the RNN hidden layer, and $\psi_{12}\left(x_k^m\right) \ldots \psi_N\left(x_k^m\right)$ are the predefined lifting functions, which take the form of Gaussian functions as:

$$\psi_i\left(x_k^m\right) = \exp\left(-\frac{\left\|x_k^m - c_i\right\|^2}{\sigma_i^2}\right), \quad i = 1, \ldots, N \tag{18}$$

where $c_i \in \mathbb{R}^n$ is the center and $\sigma_i > 0$ is the bandwidth.

The predictive performance of the model (17) is quantitatively assessed using the Root Mean Square Error (RMSE), with units of Newtons (N), defined as follows:

$$\text{RMSE} = \sqrt{\frac{1}{k_{\max}} \sum_{k=1}^{k_{\max}} \left\| F_{MR_k} - F_k^m \right\|^2} \tag{19}$$

where F_k^m and F_{MR_k} denote the output damping forces derived from Eqs. (5) and (17), respectively.

The model is evaluated across a random configuration of initial states and control inputs. Predictions are performed for 5, 10, and 20 steps by lifting the observation function to 30, 50, and 80 dimensions, respectively. The corresponding RMSE results are summarized in Table 2.

Table 2
RMSE values of the Koopman-based linear model.

Prediction Horizon	5	10	20
Koopman-30	2.29	2.31	3.48
Koopman-50	2.28	2.01	3.06
Koopman-80	2.04	2.55	2.99

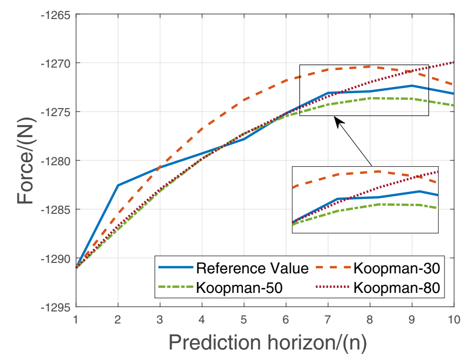

Fig. 5. Prediction results of the Koopman-based linear model.

In addition, Fig. 5 compares the prediction dynamics of the RNN model and Koopman-based linear models of varying dimensions across a 10-step prediction horizon.

The results presented in Table 2 demonstrate the high accuracy of all dimensions of the Koopman linear models across different prediction horizons, validating that the linear model (17) effectively characterizes the nonlinear dynamics of the MR damper and establishes a foundation for controller design. Furthermore, as depicted in Fig. 5, the prediction errors are maintained within 5 N, which verifies that the 30-dimensional model already satisfies the required accuracy and that further increasing the dimension yields no notable improvement. Its minimal state dimension simplifies the implementation of the H_∞/GH_2 controller gains, while the adopted control framework ensures strong robustness against modeling uncertainties and guarantees closed-loop stability. Accordingly, the 30-dimensional Koopman-based linear model is selected for the subsequent control synthesis.

Remark 4. The “globally linear representation” of the MR damper dynamics achieved through the Koopman operator is valid within the mechanically permissible operating range defined in this study. In alignment with established literature [39,40], the Koopman methodology facilitates the representation of nonlinear system dynamics in a linear form within a higher-dimensional lifted space. However, this representation may exhibit reduced fidelity under extreme operating conditions-such as abrupt variations in the rheological properties of the damping fluid, or displacement/velocity responses exceeding the mechanical design limits. This reflects an inherent constraint not only in data-driven modeling methods but also in physics-based models. The implementation of robust control strategies can partially compensate for performance degradation resulting from such model-plant mismatch.

(3) Linear model of quarter-vehicle semi-active suspension with MR dampers

An integrated linear model is established by integrating the suspension model Eq. (4) and the Koopman-based linear representation of the MR damper Eq. (17). The normalization and denormalization relations are defined in Eqs. (7) and (8).

$$\begin{cases} \chi(k+1) = G\chi(k) + H_1\left[-\xi \cdot C_{MR} \cdot z(k+1) - b\right] + H_2 w(k) \\ z(k+1) = A_{MR} \cdot z(k) + B_{MR} \cdot u^m(k) \end{cases} \tag{20}$$

It is worth noting that the damping force output from the Koopman-based linear model serves as the control input to the suspension system. This interaction forms an action–reaction pair, satisfying Newton's third law with respect to both magnitude and direction.

The conversion between the normalized and actual values is given by:

$$\begin{aligned} &I^m(k) = \varsigma_1 \cdot I(k) + d_1 \\ &\chi_1^m(k) = \varsigma_2 \cdot \kappa_1 \cdot \chi(k) + d_2 \\ &\chi_2^m(k) - \chi_4^m(k) = \varsigma_3 \cdot \kappa_2 \cdot \chi(k) + d_3 \end{aligned} \tag{21}$$

The relevant parameters are summarized in Table 3.

The subscripts max and min correspond to the predefined upper and lower bounds, respectively, all of which are fixed known constants.

Additionally,

$$d = \begin{bmatrix} d_1 & d_2 & d_3 \end{bmatrix}^{\mathrm{T}}, \kappa_1 = \begin{bmatrix} 1 & 0 & 0 & 0 & 0 & 0 \end{bmatrix}, \kappa_2 = \begin{bmatrix} 0 & 1 & 0 & -1 & 0 & 0 \end{bmatrix}.$$

From Eq. (21), system (20) can be expressed as:

$$\begin{cases} \chi(k+1) = G \cdot \chi(k) - \xi \cdot H_1 \cdot C_{MR} \cdot z(k+1) - H_1 \cdot b + H_2 \cdot w(k) \\ z(k+1) = A_{MR} \cdot z(k) + \varsigma_1 \cdot B_{MR1} \cdot I(k) + B_{MR} \cdot d \\ \qquad + \left(\varsigma_2 \cdot B_{MR2} \cdot \kappa_1 + \varsigma_3 \cdot B_{MR3} \cdot \kappa_2\right) \cdot \chi(k) \end{cases} \tag{22}$$

where $B_{MR} = \begin{bmatrix} B_{MR1} & B_{MR2} & B_{MR3} \end{bmatrix}$.

Define the augmented system as:

$$X(k) = \begin{bmatrix} \chi(k) & z(k) & 1 \end{bmatrix}^{\mathrm{T}}$$

Eq. (22) can be transformed into:

$$X(k+1) = \tilde{A}X(k) + \tilde{B}I(k) + \tilde{H}_2 w(k) \tag{23}$$

where

$$\tilde{A} = \begin{bmatrix} \tilde{A}_{11} & -\xi H_1 \cdot C_{MR} \cdot A_{MR} & -H_1 b - \xi H_1 \cdot C_{MR} \cdot \left(B_{MR} \cdot d\right) \\ \varsigma_2 \cdot B_{MR2} \cdot \kappa_1 + \varsigma_3 \cdot B_{MR3} \cdot \kappa_2 & A_{MR} & B_{MR} \cdot d \\ 0 & 0 & 1 \end{bmatrix},$$

$$\tilde{B} = \begin{bmatrix} -\xi \cdot H_1 \cdot C_{MR} \cdot \varsigma_1 \cdot B_{MR1} \\ \varsigma_1 \cdot B_{MR1} \\ 0 \end{bmatrix}, \tilde{H}_2 = \begin{bmatrix} H_2 \\ O_{30\times1} \\ 0 \end{bmatrix},$$

$$\tilde{A}_{11} = G - \xi \cdot H_1 \cdot C_{MR} \cdot \left(\varsigma_2 \cdot B_{MR2} \cdot \kappa_1 + \varsigma_3 \cdot B_{MR3} \cdot \kappa_2\right),$$

where $O_{i\times j}$ is a zero matrix of dimensions $i \times j$.

Consequently, the multi-objective optimization problem for the original nonlinear system (9) is equivalently transformed into a controller design problem for the linear system (23). Therefore, the control design complexity is significantly reduced.

According to the system control objectives, $y_1(k)$ is designated as the performance output. Based on Eq. (23), this yields:

$$y_1(k) = C_1 X(k) + D_1 I(k) \tag{24}$$

where

$$C_1 = -\frac{1}{m_s}\begin{bmatrix} c_{11} & \xi \cdot C_{MR}A_{MR} & \xi \cdot C_{MR}B_{MR} \cdot d + b \end{bmatrix}_{1\times37},$$

$$D_1 = -\frac{1}{m_s} \cdot \xi \cdot C_{MR} \cdot \varsigma_1 \cdot B_{MR1},$$

$$c_{11} = \xi \cdot C_{MR}\left(\varsigma_2 \cdot B_{MR2} \cdot \kappa_1 + \varsigma_3 \cdot B_{MR3} \cdot \kappa_2\right) + k_s \cdot \kappa_1 + c_s \cdot \kappa_2$$

The constrained system output $y_2(k)$ is defined as:

$$y_2(k) = C_2 X(k) + D_2 I(k) \tag{25}$$

where

$$C_2 = \begin{bmatrix} \frac{\kappa_1}{S_{\max}} & O_{1\times30} & 0 \\ \frac{k_t \cdot \kappa_3}{f_{\text{static}}} & O_{1\times30} & 0 \\ O_{1\times6} & O_{1\times30} & -1 \end{bmatrix}, \kappa_3 = \begin{bmatrix} 0 & 0 & 1 & 0 & 0 & 0 \end{bmatrix},$$

$$D_2 = \begin{bmatrix} 0 \\ 0 \\ 2 \end{bmatrix}$$

Table 3
Parameter definitions for the integrated Koopman-based linear model.

ς_1	ς_2	ς_3	d_1	d_2	d_3
$\frac{2}{I_{\max} - I_{\min}}$	$\frac{2}{\chi_{s\max} - \chi_{s\min}}$	$\frac{2}{\chi_{v\max} - \chi_{v\min}}$	$-\frac{I_{\max} + I_{\min}}{I_{\max} - I_{\min}}$	$-\frac{\chi_{s\max} + \chi_{s\min}}{\chi_{s\max} - \chi_{s\min}}$	$-\frac{\chi_{v\max} + \chi_{v\min}}{\chi_{v\max} - \chi_{v\min}}$

Remark 5. The control current I is bounded within $[0, 1]$A. However, the GH_2 control method requires symmetric constraints. Therefore, a transformation is applied, i.e., $2I - 1 \in [-1, 1]$A.

Remark 6. Physics-based models for MR dampers (e.g., the Bouc-Wen model) are parameter-intensive, and lack generalizability across operating conditions. In contrast, the nonlinear dynamics of the MR damper can be captured directly by RNNs from experimental data, thereby improving its adaptability to the actual system. Furthermore, to facilitate linear robust controller design, the Koopman operator is introduced to derive a globally linearized representation of the damper dynamics.

Remark 7. Although approximation errors arising from RNN training and EDMD-based projection are inherent to the modeling process, the accurate force tracking capability of the RNN model ensures that the resulting Koopman linear model can effectively capture the dynamic characteristics of the MR damper, which has been validated through a testbed in our previous work [41].

3.3. Static output-feedback H_∞/GH_2 controller design

This section focuses on the development of a static output-feedback H_∞/GH_2 controller based on the linearized IWM driven MR semi-active suspension system described in Eq. (23). The controller is designed with the objective of maintaining closed-loop stability while fulfilling the aforementioned control objectives, thereby coordinating control performance with constraint requirements.

Define G_{wy_1} as the closed-loop transfer function mapping the road excitation w to the performance output y_1, and T_{wy_2} as the one from w to the constrained output y_2. Accordingly, the control objective can be described as:

$$\begin{aligned} &\text{minimize} \quad \left\|G_{wy_1}\right\|_\infty \\ &\text{s.t.} \quad \left\|T_{wy_2}\right\|_g < 1 \end{aligned} \tag{26}$$

while

$$\left\|G_{wy_1}\right\|_\infty := \sup_{w(t)\in L_2} \frac{\|y_1\|_2}{\|w\|_2} < \rho \tag{27}$$

$$\left\|T_{wy_2}\right\|_g := \sup_{w\in L_2} \frac{\|y_2\|_\infty}{\|w\|_2} < 1 \tag{28}$$

and the infinity norm of the constrained system output y_2 is:

$$\|y_2\|_\infty := \max_{i=1,2,\ldots,n} \sup_{t\geq 0} |y_{2i}| \tag{29}$$

The static output-feedback control law is defined as:

$$I(k) = K y_3(k) \tag{30}$$

while

$$y_3(k) = C_3 X(k) \tag{31}$$

$$C_3 = \begin{bmatrix} c_{31} & O_{2\times 30} & O_{2\times 1} \end{bmatrix}, c_{31} = \begin{bmatrix} 1 & 0 & 0 & 0 & 0 & 0 \\ 0 & 1 & 0 & -1 & 0 & 0 \end{bmatrix}$$

Substituting controller Eq. (30) into system (23), the controlled output (24), and the constrained output (25), respectively, yields the following closed-loop system:

$$\begin{aligned} X(k+1) &= \tilde{A}X(k) + \tilde{B}I(k) + \tilde{H}_2 w(k) \\ &= \left(\tilde{A} + \tilde{B}\cdot K\cdot C_3\right)X(k) + \tilde{H}_2 w(k) \end{aligned} \tag{32}$$

$$\begin{aligned} y_1(k) &= C_1 X(k) + D_1 I(k) \\ &= \left(C_1 + D_1\cdot K\cdot C_3\right)X(k) \end{aligned} \tag{33}$$

$$y_2(k) = \left(C_2 + D_2\cdot K\cdot C_3\right)X(k) \tag{34}$$

Theorem 1. *Assume $x(0) = 0$, the following two conditions are mathematically equivalent: 1) the closed-loop system described by Eq. (32) is asymptotically stable, with its H_∞ norm from $w(k)$ to the control output $y_1(k)$ is bounded by a given positive scalar ρ, and its GH_2 norm from $w(k)$ to the constraint output $y_2(k)$ is less than 1; 2) there exist positive definite symmetric matrices $W_k = W_{k+1} \in \mathbb{R}^{37\times 37}$ and $S_k \in \mathbb{R}^{1\times 2}$ satisfying the following condition:*

$$\text{minimize } \rho^2$$

$$\begin{bmatrix} -W_k & * & * & * \\ 0 & -\rho^2\mathfrak{I}_{1*1} & * & * \\ \tilde{A}W_k + \tilde{B}S_k C_3 & \tilde{H}_2 & -W_{k+1} & * \\ C_1 W_k + D_1 S_k C_3 & 0 & 0 & -\mathfrak{I}_{1*1} \end{bmatrix} < 0 \tag{35}$$

$$\begin{bmatrix} -W_k & * \\ C_2\cdot W_k + D_2\cdot S_k\cdot C_3 & -\mathfrak{I}_{3*3} \end{bmatrix} < 0 \tag{36}$$

If the optimal solution $\left(\rho^*, W_k^*, S_k^*\right)$ exists, the controller gain can be obtained as follows:

$$K = S_k \cdot N_k^{-1} \tag{37}$$

where $N_k C_3 = C_3 W_k$, $\mathfrak{I}$ denotes the identity matrix with compatible dimensions.

Proof:

(i) The H_∞ performance of the system is first analyzed.

The performance requirement in (26) can be ensured if the following inequality is satisfied for all k:

$$V(X(k+1)) - V(X(k)) + y_1^{\mathrm{T}}(k)y_1(k) - \rho^2 w^{\mathrm{T}}(k)w(k) < 0 \tag{38}$$

Then, (38) can be reformulated as:

$$X^{\mathrm{T}}(k+1)P_{k+1}X(k+1) - X^{\mathrm{T}}(k)P_k X(k) + y_1^{\mathrm{T}}(k)y_1(k) - \rho^2 w^{\mathrm{T}}(k)w(k) < 0 \tag{39}$$

where positive-definite symmetric matrices satisfy $P_{k+1} = P_k$.

Furthermore, (39) can be equivalently expressed as follows:

$$\begin{bmatrix} X(k) \\ w(k) \end{bmatrix}^{\mathrm{T}} \begin{bmatrix} -P_k & 0 \\ 0 & -\rho^2 \end{bmatrix} \begin{bmatrix} X(k) \\ w(k) \end{bmatrix} + X^{\mathrm{T}}(k+1)P_{k+1}X(k+1) + y_1^{\mathrm{T}}(k)y_1(k) < 0 \tag{40}$$

By applying the Schur complement twice to the inequality (40), the following LMI is derived:

$$\begin{bmatrix} -P_k & * & * & * \\ 0 & -\rho^2\mathfrak{I}_{1*1} & * & * \\ \tilde{A} + \tilde{B}\cdot K\cdot C_3 & \tilde{H}_2 & -P_{k+1}^{-1} & * \\ C_1 + D_1\cdot K\cdot C_3 & 0 & 0 & -\mathfrak{I}_{1*1} \end{bmatrix} < 0 \tag{41}$$

Since Eq. (41) contains P_{k+1}^{-1}, it cannot be directly solved as an LMI. Accordingly, the following linearization method is employed.

Pre- and post-multiplying both sides of the inequality (41) by $\operatorname{diag}\left\{ P_k^{-1} \quad \mathfrak{I} \quad \mathfrak{I} \quad \mathfrak{I} \right\}$, and introducing the substitution $W_k = P_k^{-1}$, leads to the equivalent form:

$$\begin{bmatrix} -W_k & * & * & * \\ 0 & -\rho^2\mathfrak{I}_{1*1} & * & * \\ \left(\tilde{A} + \tilde{B}\cdot K\cdot C_3\right)W_k & \tilde{H}_2 & -W_{k+1} & * \\ \left(C_1 + D_1\cdot K\cdot C_3\right)W_k & 0 & 0 & -\mathfrak{I}_{1*1} \end{bmatrix} < 0 \tag{42}$$

Furthermore, denote

$$\begin{aligned} N_k C_3 &= C_3 W_k \\ S_k &= K\cdot N_k \end{aligned} \tag{43}$$

Then inequality (42) can be transformed into (35), which implies that the H_∞ norm from $w(t)$ to $y_1(k)$ is bounded by ρ^*. Thereby the proof is completed.

(ii) The GH_2 performance of the system will be analyzed next.

For any positive integer $\Bbbk$, define

$$J(\Bbbk) = V(X(\Bbbk)) - \sum_{k=0}^{\Bbbk-1} w^{\mathrm{T}}(k)w(k) \tag{44}$$

Then for any sequence $w(k) \neq 0 \in \ell_2[0,\infty)$, and $k \in \{1, 2, \cdots \Bbbk - 1\}$, with $X(0) = 0$, we have

$$\begin{aligned} J(\Bbbk) &= \sum_{k=0}^{\Bbbk-1}\left[\left(V(X(k+1)) - V(X(k))\right) - w^{\mathrm{T}}(k)w(k)\right] \\ &= \sum_{k=0}^{\Bbbk-1}\begin{bmatrix} X(k) \\ w(k) \\ 1 \end{bmatrix}^{\mathrm{T}} \begin{bmatrix} -P_k & * & * \\ 0 & -\mathfrak{I}_{1*1} & * \\ \tilde{A} + \tilde{B}\cdot K\cdot C_3 & \tilde{H}_2 & -P_{k+1}^{-1} \end{bmatrix} \begin{bmatrix} X(k) \\ w(k) \\ 1 \end{bmatrix} \end{aligned} \tag{45}$$

Therefore, $J(\Bbbk) < 0$ holds if

$$\begin{bmatrix} -P_k & * & * \\ 0 & -\Im_{1*1} & * \\ \tilde{A} + \tilde{B} \cdot K \cdot C_3 & \tilde{H}_2 & -P_{k+1}^{-1} \end{bmatrix} < 0 \tag{46}$$

The presence of the term P_{k+1}^{-1} in inequality (46) prevents the problem from being directly formulated using the LMI toolbox. Consequently, an appropriate linearization should be introduced to reformulate the inequality into an LMI-compatible form.

Pre- and post-multiplying both sides of (46) by $\operatorname{diag}\{\ P_k^{-1} \quad \Im \quad \Im\ \}$, and introducing the substitution $W_k = P_k^{-1}$, leads to the equivalent form:

$$\begin{bmatrix} -W_k & * & * \\ 0 & -\Im_{1*1} & * \\ \tilde{A} \cdot W_k + \tilde{B} \cdot S_k \cdot C_3 & \tilde{H}_2 & -W_{k+1} \end{bmatrix} < 0 \tag{47}$$

For any $w(k) \neq 0 \in \ell_2[0, \infty)$, it satisfies:

$$V(X(\Bbbk)) < \sum_{k=0}^{\Bbbk-1} w^{\mathrm{T}}(k) w(k) \tag{48}$$

For any $\Bbbk$, define

$$y_2^{\mathrm{T}}(\Bbbk) y_2(\Bbbk) < X^{\mathrm{T}}(\Bbbk) P_k X(\Bbbk) \tag{49}$$

According to the Schur complement, (49) is equivalent to:

$$\begin{bmatrix} -P_k & * \\ C_2 + D_2 \cdot K \cdot C_3 & -\Im_{3*3} \end{bmatrix} < 0 \tag{50}$$

Pre- and post-multiplying both sides of (50) by $\operatorname{diag}\{\ P_k^{-1} \quad \Im\ \}$, and introducing the substitution $W_k = P_k^{-1}$, leads to:

$$\begin{bmatrix} -W_k & * \\ \left(C_2 + D_2 \cdot K \cdot C_3\right) \cdot W_k & -\Im_{3*3} \end{bmatrix} < 0 \tag{51}$$

Since $N_k C_3 = C_3 W_k$, $S_k = K \cdot N_k$, the above inequality yields:

$$\begin{bmatrix} -W_k & * \\ C_2 \cdot W_k + D_2 \cdot S_k \cdot C_3 & -\Im_{3*3} \end{bmatrix} < 0 \tag{52}$$

From inequalities (48), (49), and (52), we obtain

$$y_2^{\mathrm{T}}(\Bbbk) y_2(\Bbbk) < \sum_{k=0}^{\Bbbk-1} w^{\mathrm{T}}(k) w(k) \tag{53}$$

From Eq. (28), it can be concluded that if inequalities (36) and (47) are satisfied, then for any $\Bbbk$, the closed-loop GH_2 norm of the transfer function from the excitation $w(t)$ to the constrained output $y_2(t)$ is less than 1. Furthermore, since inequality (47) is subsumed by (35), it is sufficient to satisfy inequality (36) alone.

4. Simulation analysis

The proposed Koopman-based static output feedback H_∞/GH_2 controller is applied to an IWM driven semi-active suspension system equipped with MR dampers. To validate the effectiveness of the integrated control strategy, a comparative analysis is conducted against the PASOF-H_∞/GH_2 method proposed in [42] and a conventional Sky-hook control method.

The evaluation covers corrugated, random and abrupt road profiles, using the parameters listed in Table 1. For the PASOF-H_∞/GH_2 control method, the number of segments is set to 15. Table 4 presents the RMS values of the vertical acceleration under different road excitations, providing a quantitative measure of ride comfort across varied operating conditions.

Table 4
RMS values of vertical body acceleration under various road excitations.

Road Excitation	Speed (m/s)	Koopman-H_∞/GH_2	PASOF-H_∞/GH_2	Sky-hook
Corrugated Road	5	1.8894	1.9674	2.1647
Class C Random Road	20	1.5738	1.7024	1.8447
Abrupt Excitation	8	0.7141	1.1628	0.9130

4.1. Performance evaluation under standard road profiles

(1) Corrugated Road

The road excitation induced by a corrugated road with N periodic bumps is modeled by the following mathematical expression:

$$x_r\left(t; t_{(0,j)}\right) = \sum_{j=1}^{N} \frac{\hat{A}}{2}\left(1 - \cos\left(\frac{2\pi v\left(t - t_{(0,j)}\right)}{L}\right)\right) 1_{\left[t_{(0,j)}, t_{(0,j+L/v)}\right]}(t) \tag{54}$$

where $t_{(0,j)}$ is the start time of the $j-th$ bump; $1_{\left[t_{(0,j)}, t_{(0,j+L/v)}\right]}(t)$ is the interval indicator function, which is defined as:

$$1_{\left[t_{(0,j)}, t_{(0,j+L/v)}\right]}(t) = \begin{cases} 1 & \text{if } t \in \left[t_{(0,j)}, t_{(0,j+L/v)}\right] \\ 0 & \text{otherwise} \end{cases}$$

When the vehicle passes at a constant speed of $v = 5$m/s over a corrugated road, the time-domain responses of the IWM driven semi-active suspension system under three control strategies are compared in Fig. 6. The road profile consists of periodic bumps with a height of $\hat{A} = 0.04$m, a length of $L = 0.6$m, and a spacing of 0.6m.

The simulation results presented in Fig. 6(a) and Table 4 indicate that the proposed Koopman-H_∞/GH_2 controller substantially enhances the ride comfort of the vehicle. Specifically, it reduces the body vertical acceleration RMS to 1.8894, compared to 1.9674 for the PASOF-H_∞/GH_2 controller, representing a performance improvement of approximately 3.96%. Furthermore, the enhancement is more substantial when compared to the classical Sky-hook method, with a significant improvement of about 12.72%.

In addition, the PASOF-H_∞/GH_2 controller exhibits an increased vibration frequency compared to the other two methods, revealing a fundamental drawback of the piecewise linearization strategy: insufficient smoothing across segment boundaries. This leads to frequent controller switching under dynamic excitations, which generates considerable oscillatory behavior.

Furthermore, the peak response reflects the maximal transient impact experienced by the suspension system under different road excitations. As shown in Table 5, under corrugated road excitation, the proposed Koopman-H_∞/GH_2 controller exhibits a peak acceleration of 4.7055 $\mathrm{m/s^2}$ at 0.78 s. Although this value is slightly higher than that of the PASOF-H_∞/GH_2 controller (4.1901 $\mathrm{m/s^2}$ at 0.46 s), as shown in Fig. 6(a), its vibration frequency is significantly lower, suggesting a reduction in oscillatory behavior. In contrast, the Sky-hook controller achieves the highest peak acceleration of 5.1452 $\mathrm{m/s^2}$ at only 0.12 s, demonstrating its limited effectiveness in attenuating transient shock loads.

As illustrated in Fig. 6(b), the suspension stroke constraint is strictly satisfied by all three control strategies. However, Fig. 6(c) demonstrates a critical divergence in the dynamic-to-static tire load ratio. The responses of both PASOF-H_∞/GH_2 and Sky-hook control exceed the prescribed limit, thereby compromising driving safety. In contrast, the Koopman-H_∞/GH_2 controller ensures consistent adherence to the safety constraint.

The damping force outputs of the Koopman-H_∞/GH_2 and PASOF-H_∞/GH_2 controllers under corrugated road excitation are compared in Fig. 7.

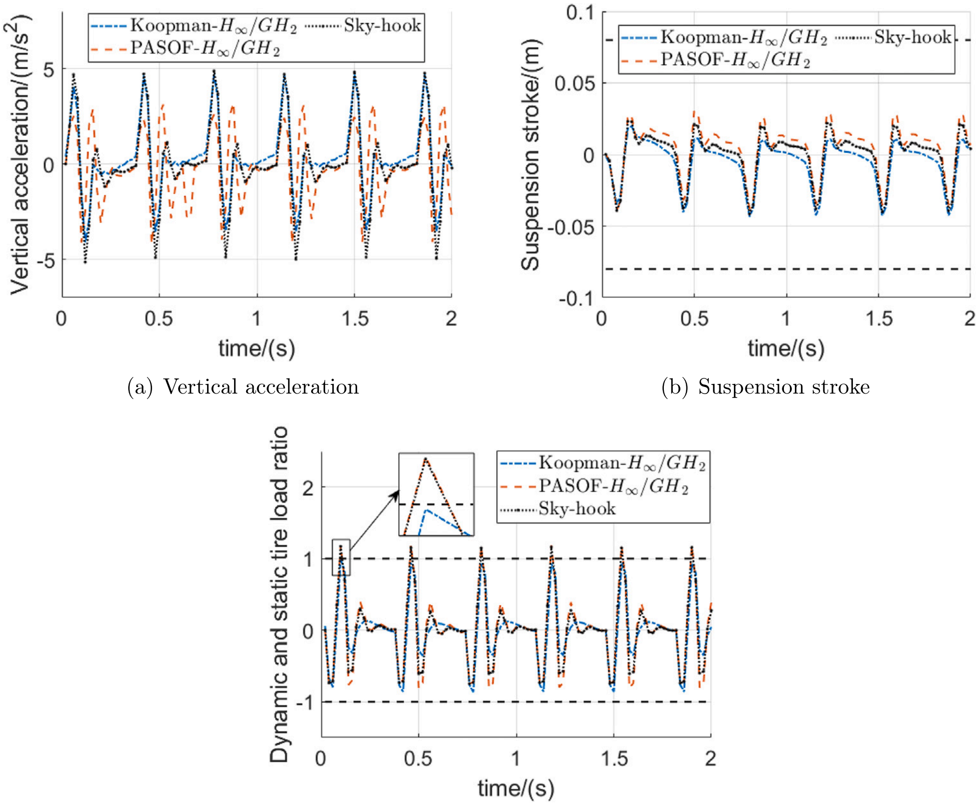

(a) Vertical acceleration

(b) Suspension stroke

(c) Dynamic-to-static tire load ratio

Fig. 6. Dynamic response of the suspension system under corrugated road excitation.

Table 5
Time-domain analysis of absolute peak response under corrugated road.

Control Strategy	Peak time (s)	Peak (m/s^2)
Koopman-H_∞/GH_2	0.78	4.7055
PASOF-H_∞/GH_2	0.46	4.1901
Sky-hook	0.12	5.1452

Fig. 7(a) shows that the Koopman-H_∞/GH_2 controller fully complies with the energy dissipation characteristics of the MR damper. In contrast, Fig. 7(b) reveals that the PASOF-H_∞/GH_2 control strategy exhibits a more intense response, and requires further optimization.

Finally, the damping force output of a conventional H_∞ controller which ignores the physical constraints of the MR damper, is shown in Fig. 8. It is evident that the resulting control force frequently violates the inherent energy dissipation principles of the MR damper, consequently resulting in the deterioration and even failure of the overall system response.

Remark 8. As systematically investigated in our prior work [42], increasing the number of segments in piecewise affine systems does not monotonically improve performance. Under identical conditions, the 15-segment configuration achieves the best trade-off between model complexity and control effectiveness compared to 9- and 21-segment alternatives, and is therefore adopted herein.

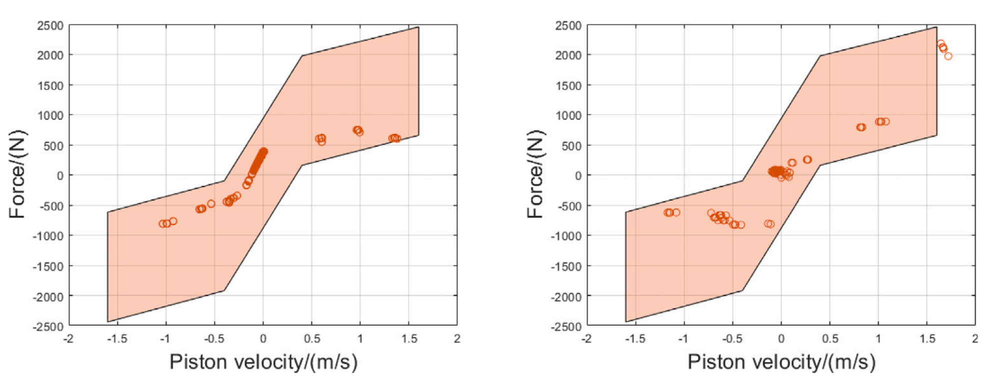

(a) Koopman-H_∞/GH_2

(b) PASOF-H_∞/GH_2

Fig. 7. Comparison of constrained damping force under corrugated road excitation.

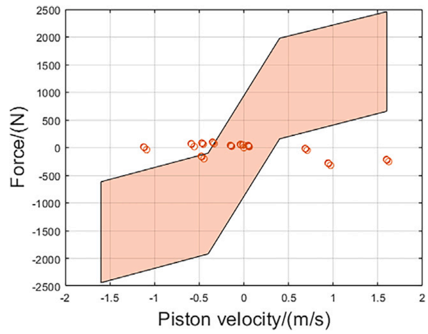

Fig. 8. Unconstrained damping force of conventional H_∞ control under corrugated road excitation.

(2) Class C Random Road

The dynamic response of the system when subjected to a C-class random road input at a constant speed of 20 m/s is given in Fig. 9.

As depicted in Fig. 9(a) and Table 4, the Koopman-H_∞/GH_2 controller demonstrates a performance improvement in vertical acceleration control of approximately 7.55% and 14.69% over the PASOF-H_∞/GH_2 and Sky-hook control methods, respectively.

Additionally, as shown in Table 6, under Class C random road excitation, the proposed controller produces a peak acceleration of 3.7115 m/s^2, which is lower than both the PASOF-H_∞/GH_2 controller (4.3767 m/s^2) and the Sky-hook controller (4.2927 m/s^2). This result demonstrates the enhanced damping capability of the proposed control strategy.

As shown in Fig. 9(b), all three control strategies satisfy the suspension stroke constraint, thereby ensuring structural safety. However, Fig. 9(c) reveals that the dynamic-to-static tire load ratio occasionally exceeds the prescribed limit under both PASOF-H_∞/GH_2 and Sky-hook control. In contrast, the proposed Koopman-H_∞/GH_2 controller consistently adheres to this constraint.

Table 6
Time-domain analysis of absolute peak response under class C random road.

Control Strategy	Peak time (s)	Peak (m/s^2)
Koopman-H_∞/GH_2	0.38	3.7115
PASOF-H_∞/GH_2	1.58	4.3767
Sky-hook	1.32	4.2927

Furthermore, as shown in Fig. 10, the damping forces generated by both the Koopman-H_∞/GH_2 and PASOF-H_∞/GH_2 controllers remain within the physical capabilities of the MR damper.

As shown in Fig. 11, the conventional H_∞ controller neglects the energy dissipation characteristics of the MR damper. This oversight creates a significant gap between its theoretical design and practical implementation.

4.2. Robustness assessment of abrupt excitation with parameter perturbations

To evaluate the robustness and adaptive capability of the proposed control algorithm under extreme operating conditions, a model parameter perturbation is introduced in the simulation. This perturbation emulates performance degradation caused by variations in temperature or changes in the medium, resulting in a mismatch between the Koopman-based linear model and the physical system. It is realized by superimposing an uniformly distributed multiplicative error over the interval [−20%, 20%] onto the nominal damping force output $F(k)$ in Eq. (4). Consequently, the actual output damping force $F_p(k)$ is then expressed as:

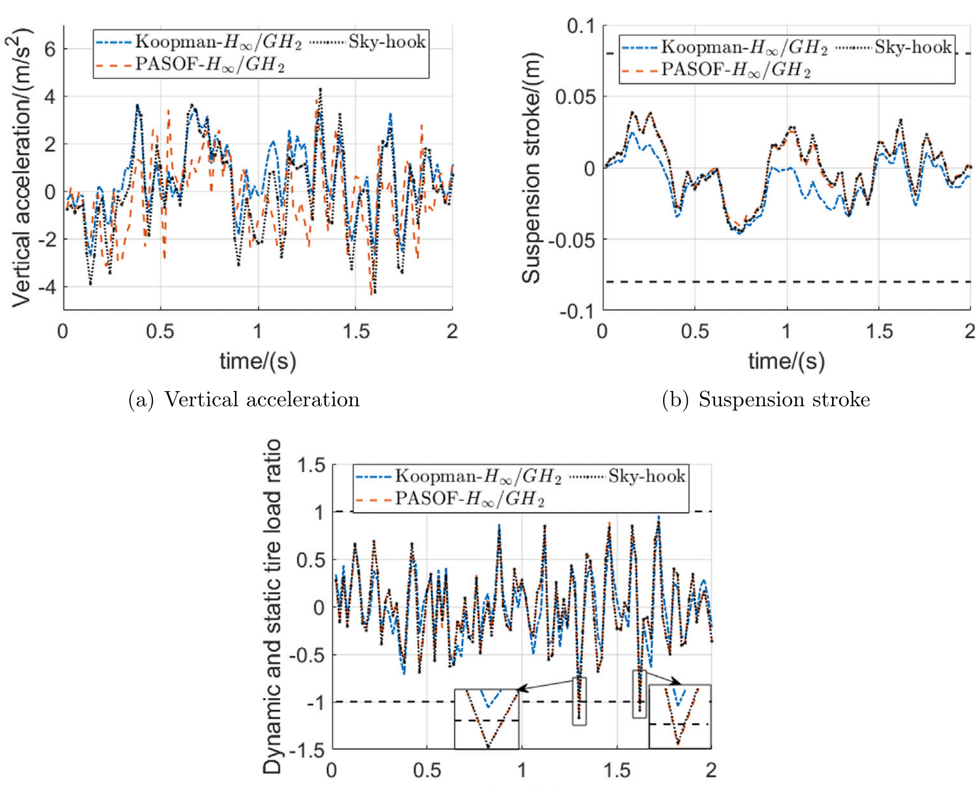

(a) Vertical acceleration (b) Suspension stroke

(c) Dynamic-to-static tire load ratio

Fig. 9. Dynamic responses of the suspension system under random road excitation.

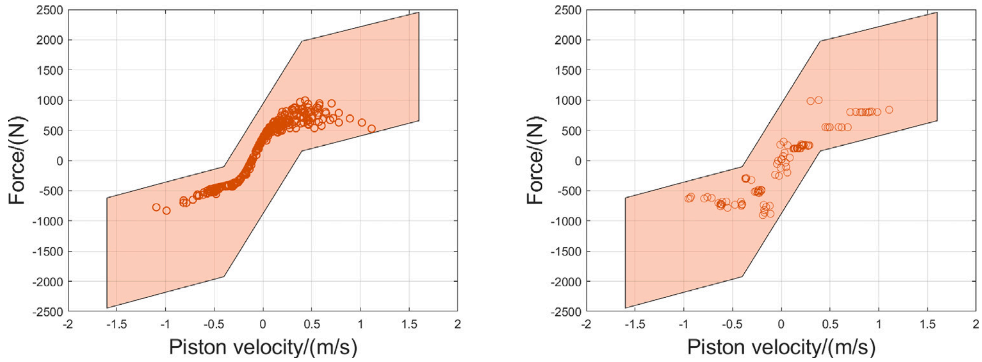

(a) Koopman-H_∞/GH_2 (b) PASOF-H_∞/GH_2

Fig. 10. Comparison of constrained damping forces under random road excitation.

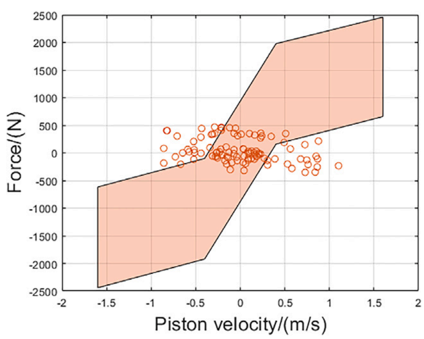

Fig. 11. Unconstrained damping force of conventional H_∞ control under random road excitation.

$$F_p(k) = (0.8 + (1.2 - 0.8) \cdot rand()) \cdot F(k) \tag{55}$$

Specifically, an increase in temperature reduces the viscosity of the base fluid, while sedimentation decreases the concentration of effective magnetic particles in the suspension. Both factors weaken the MR effect, consequently producing a lower actual damping force than the controller anticipates. This setup realistically emulates actuator degradation in real-world environments caused by performance deterioration. The reverse effect induced by a decrease in temperature follows a similar pattern.

As shown in Fig. 12(d), the road excitation, characterized by a Class-B random road superimposed with a pothole occurring at $t_0 = 1$s, has an amplitude of 0.04m and a length of 1m. Assuming the vehicle

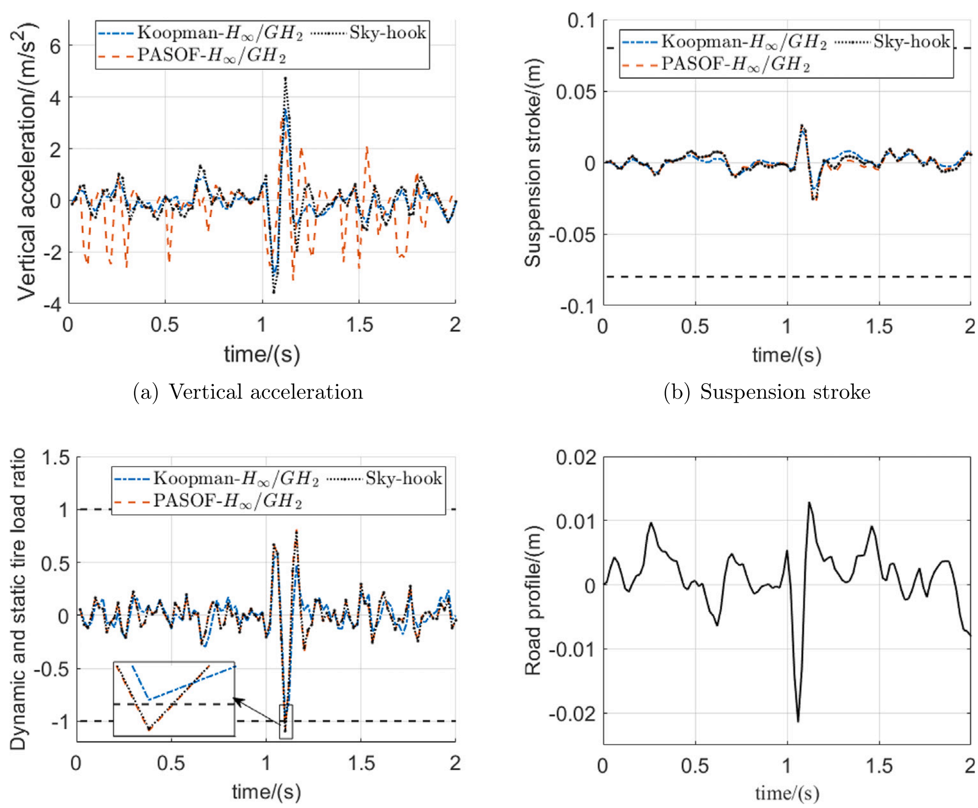

(a) Vertical acceleration (b) Suspension stroke

(c) Dynamic-to-static tire load ratio (d) Class-B random road superimposed with a pothole

Fig. 12. Dynamic responses of the suspension system under abrupt excitation.

Table 7
Time-domain analysis of absolute peak response under abrupt excitation.

Control Strategy	Peak time (s)	Peak (m/s^2)
Koopman-H_∞/GH_2	1.12	3.5637
PASOF-H_∞/GH_2	1.10	3.2696
Sky-hook	1.12	4.7256

passes at a constant speed of $v = 8\text{m/s}$, the time-domain responses of the IWM-driven semi-active suspension system under three control strategies are compared in Fig. 12(a)–(c).

As presented in Fig. 12(a) and Table 4, the Koopman-H_∞/GH_2 control strategy significantly improves ride comfort compared to the PASOF-H_∞/GH_2 and Sky-hook strategies, with performance enhancements of approximately 38.59% and 21.79%, respectively.

Moreover, as shown in Table 7, under abrupt excitation, the proposed controller yields a peak acceleration of 3.5637 m/s^2, which is notably lower than that of the Sky-hook controller (4.7256 m/s^2), albeit slightly higher than that of the PASOF-H_∞/GH_2 controller (3.2696 m/s^2). This result demonstrates the effectiveness of the proposed method in suppressing peak vibration responses induced by abrupt road disturbances.

Fig. 12(b) shows that all three control strategies effectively maintain the suspension stroke within its required constraint. However, as shown in Fig. 12(c), the PASOF-H_∞/GH_2 and Sky-hook control strategies frequently violate the constraint on driving safety. In contrast, the Koopman-H_∞/GH_2 controller successfully keeps it within the allowable range.

Furthermore, Fig. 13(b) reveals that the PASOF-H_∞/GH_2 strategy, due to its inherent limitations, ultimately compromises the overall suspension performance. In comparison, the Koopman-H_∞/GH_2 strategy remains strictly within the physical limitations of the MR damper, and achieves a better balance between ride comfort and driving safety.

Fig. 14 presents the damping force range of a conventional H_∞ controller designed without considering the dissipation characteristics of the MR damper, thereby producing a non-physical response and resulting in complete system failure.

The simulation results show that the PASOF-H_∞/GH_2 control strategy exhibits limitations in force distribution under aggressive road excitations due to its pre-defined, fixed switching logic. In contrast, the Koopman-H_∞/GH_2 control constructs a globally linear model in a lifted space via the Koopman operator, which enables continuous force coordination and achieves a superior compromise between comfort and safety. Furthermore, parameter perturbations are effectively managed by the Koopman-H_∞/GH_2 controller, which leads to significantly enhanced robustness against uncertainties and variations in system dynamics.

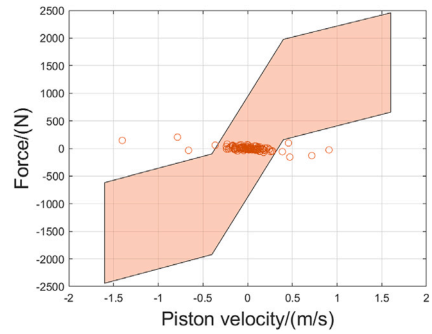

Fig. 14. Unconstrained damping force of conventional H_∞ control under abrupt excitation.

Remark 9. It is assumed that the lower-level controller in the hierarchical framework can accurately track the desired damping force generated by the PASOF-H_∞/GH_2 approach, with robustness to parameter perturbations.

5. Conclusion

A novel integrated Koopman-H_∞/GH_2 control method for IWM driven semi-active suspensions equipped with MR dampers was proposed in this paper. This method effectively addresses the optimal control problem for constrained nonlinear systems. It overcomes the approximation limitations of hierarchical control in handling dissipative nonlinear constraints, while also circumventing the rigid static switching logic inherent in piecewise affine controllers within segmented control architectures. This enables the proposed method to better exploit the adjustability of MR dampers. Simulation results demonstrated that, compared with the PASOF-H_∞/GH_2 and conventional Sky-hook control strategies, a well-balanced trade-off among ride comfort, driving safety, suspension stroke limitation, and actuator saturation constraints was achieved by the proposed approach.

To further improve the overall dynamic performance and adaptability of the system, future research will explore the integration of preview technologies and Kalman filter-based state feedback, utilizing road profile information to optimize vehicle performance. Furthermore, the coupling between electromagnetic motor forces and the suspension system has not been addressed in this study. Future work could establish a coupled dynamic model to analyze the influence of motor electromagnetic dynamics on suspension behavior and explore co-optimization strategies for integrated motor-suspension control.

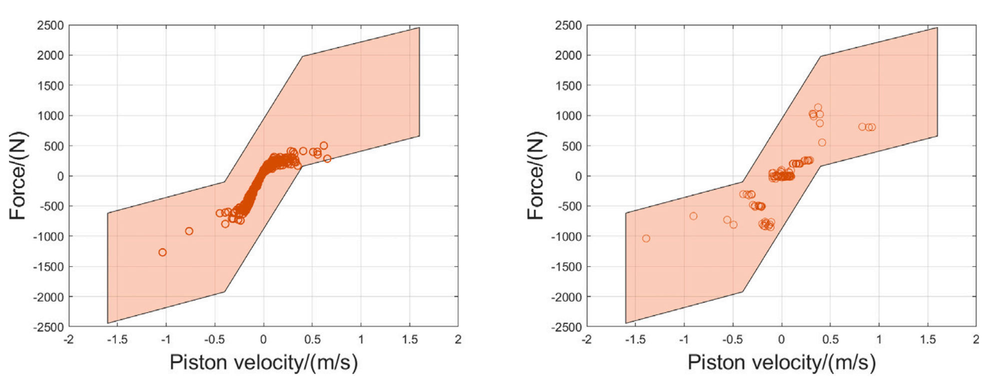

(a) Koopman-H_∞/GH_2 (b) PASOF-H_∞/GH_2

Fig. 13. Comparison of constrained damping forces under abrupt excitation.

CRediT authorship contribution statement

Jie Guo: Writing – review & editing, Writing – original draft, Validation, Software, Methodology. **Shuyou Yu:** Supervision. **Chao Ma:** Writing – review & editing.

Explicitly state

This paper is neither under consideration nor already published in another venue.

Declaration of Competing Interest

The authors declare that they have no known competing financial interests or personal relationships that could have appeared to influence the work reported in this paper.

Acknowledgements

This work was supported in part by the National Natural Science Foundation of China under Grant No. 62473167, and the Natural Science Foundation of Jilin Province No. 20240402079GH.

References

[1] Mishra S, Varshney A, Singh B, et al. Driving-cycle-based modeling and control of solar-battery-fed reluctance synchronous motor drive for light electric vehicle with energy regeneration. IEEE Trans Ind Appl 2022;58(5):6666–75.
[2] Cai S, Kirtley J, Lee C. Critical review of direct-drive electrical machine systems for electric and hybrid electric vehicles. IEEE Trans Energy Convers 2022;37(4):2657–68.
[3] Jin X, Wang J, Yan Z, et al. Robust vibration control for active suspension system of in-wheel-motor-driven electric vehicle via μ-synthesis methodology. J Dyn Syst Meas Control 2022;144(5):051007.
[4] Mahmouditabar F, Vahedi A, Takorabet N. Design and analysis of interior permanent magnet motor for electric vehicle application considering irreversible demagnetization. IEEE Trans Ind Appl 2022;58(1):284–93.
[5] Yamada S, Beauduin T, Fujimoto H, et al. Active model-based suppression of secondary ride for electric vehicles with in-wheel motors. IEEE/ASME Trans Mechatron 2022;27(6):5637–46.
[6] Yan S, Sun W. Self-powered suspension criterion and energy regeneration implementation scheme of motor-driven active suspension. Mech Syst Signal Process 2017;94:297–311.
[7] Nagaya G, Wakao Y, Abe A. Development of an in-wheel drive with advanced dynamic-damper mechanism. JSAE Rev 2003;24(4):477–81.
[8] Jin X, Wang J, He X, et al. Improving vibration performance of electric vehicles based on in-wheel motor-active suspension system via robust finite frequency control. IEEE Trans Intell Transp Syst 2023;24(2):1631–43.
[9] Shao X, Naghdy F, Du H. Reliable fuzzy H_∞ control for active suspension of in-wheel motor driven electric vehicles with dynamic damping. Mech Syst Signal Process 2017;87:365–83.
[10] Vidal V, Stano P, Tavolo G, et al. On pre-emptive in-wheel motor control for reducing the longitudinal acceleration oscillations caused by road irregularities. IEEE Trans Veh Technol 2022;71(9):9322–37.
[11] Ahmad I, Ge X, Han Q. Decentralized dynamic event-triggered communication and active suspension control of in-wheel motor driven electric vehicles with dynamic damping. IEEE/CAA J Autom Sin 2021;8(5):971–86..
[12] Li W, Zhao J, Wong PK, et al. Adaptive event-triggered fuzzy security control for active suspensions of in-wheel-motor-driven electric vehicles with probabilistic actuator attacks. IEEE Trans Transp Electrif 2025;11.
[13] Yu Z, Luo R, Wu P, et al. Robust finite-frequency vibration control of in-wheel motor driving vehicles based on torque coordination and motor suspension. IEEE Trans Transp Electrif 2025;11.
[14] Li W, Xie Z, Zhao J, et al. Static-output-feedback based robust fuzzy wheelbase preview control for uncertain active suspensions with time delay and finite frequency constraint. IEEE/CAA J Autom Sin 2021;8(3):664–78.
[15] Yang J, Ning D, Sun S, et al. A semi-active suspension using a magnetorheological damper with nonlinear negative-stiffness component. Mech Syst Signal Process 2021;147:107071.
[16] Deng L, Sun S, Christie M, et al. Investigation of a seat suspension installed with compact variable stiffness and damping rotary magnetorheological dampers. Mech Syst Signal Process 2022;171:108802.
[17] Zhang H, Cheng K, Wang E, et al. Nonlinear behaviors of a half-car magnetorheological suspension system under harmonic road excitation. IEEE Trans Veh Technol 2023;72.
[18] Emura J, Kakizaki S, Yamaoka F, et al. Development of the semi-active suspension system based on the Sky-Hook damper theory. SAE Trans 1994;103.
[19] Val S, Novak M, Sika Z, et al. Extended Ground-Hook-New concept of semi-active control of truck's suspension. Veh Syst Dyn 1997;27(5–6):289–303.
[20] Ahmadian M, Pare C. A quarter-car experimental analysis of a lternative semiactive control methods. J Intell Mater Syst Struct 2000;11(8):604–12.
[21] Nguyen M, Canale M, Sename O, et al. A model predictive control approach for semi-active suspension control problem of a full car. In: 2016 IEEE 55th conference on decision and control (CDC). Las Vegas, NV, USA; 2016. p. 721–6.
[22] Yoon D, Kim G, Choi S. Response time of magnetorheological dampers to current inputs in a semi-active suspension system: modeling, control and sensitivity analysis. Mech Syst Signal Process 2021;146.
[23] Savaia G, Sohn Y, Formentin S, et al. Experimental automatic calibration of a semi-active suspension controller via Bayesian optimization. Control Eng Pract 2021;112:104826.
[24] Ma X, Wong P, Zhao J. Practical multi-objective control for automotive semi-active suspension system with nonlinear hydraulic adjustable damper. Mech Syst Signal Process 2019;117:667–88.
[25] Nguyen S, Lam B, Ngo V. Fractional-order sliding-mode controller for semi-active vehicle MRD suspensions. Nonlinear Dyn 2020;101:795–821.
[26] Kim J, Lee T, Kim C, et al. Model predictive control of a semi-active suspension with a shift delay compensation using preview road information. Control Eng Pract 2023;137.
[27] Morato M, Nguyen M, Sename O, et al. Design of a fast real-time LPV model predictive control system for semi-active suspension control of a full vehicle. J Frankl Inst 2019;356:1196–224.
[28] Canale M, Milanese M, Novara C. Semi-active suspension control using 'fast' model-predictive techniques. IEEE Trans Control Syst Technol 2006;14(6):1034–46.
[29] Wu J, Zhou H, Liu Z, et al. A load-dependent PWA-H_∞ controller for semi-active suspensions to exploit the performance of MR dampers. Mech Syst Signal Process 2019;127:441–62.
[30] Wu J, Zhou H, Liu Z, et al. Ride comfort optimization via speed planning and preview semi-active suspension control for autonomous vehicles on uneven roads. IEEE Trans Veh Technol 2020;69(8):8343–55.
[31] Rathai K, Sename O, Alamir M. GPU-based parameterized NMPC scheme for control of half car vehicle with semi-active suspension system. IEEE Control Syst Lett 2019;3(3):631–6.
[32] Pang H, Liu F, Xu Z. Variable universe fuzzy control for vehicle semi-active suspension system with MR damper combining fuzzy neural network and particle swarm optimization. Neurocomputing 2018;306:130–40.
[33] Lee D, Jin S, Lee C. Deep reinforcement learning of semi-active suspension controller for vehicle ride comfort. IEEE Trans Veh Technol 2023;72(1):327–39.
[34] Yu S, Guo J, Xu X, et al. A cascaded control strategy for magnetorheological dampers based on Hammerstein model. Mech Syst Signal Process 2025;222:111748.
[35] Xiao Y, Zhang X, Xu X, et al. Deep neural networks with Koopman operators for modeling and control of autonomous vehicles. IEEE Trans Intell Veh 2022;8(1):135–46.
[36] Liu L, Sun M, Wang R, et al. Finite-time neural control of stochastic active electromagnetic suspension system with actuator failure. IEEE Trans Intell Veh 2024;10.
[37] Netto M, Susuki Y, Mili L. Data-driven participation factors for nonlinear systems based on Koopman mode decomposition. IEEE Control Syst Lett 2019;3(1):198–203.
[38] Korda M, Mezić I. Linear predictors for nonlinear dynamical systems: Koopman operator meets model predictive control. Automatica 2018;93:149–60.
[39] Koopman BO. Hamiltonian systems and transformation in Hilbert space. Proc Natl Acad Sci 1931;17(5):315–8.
[40] Mezic I. Spectral properties of dynamical systems, model reduction and decompositions. Nonlinear Dyn 2005;41:309–25.
[41] Liu Z, Xu X, Guo J, et al. Damping force tracking control of magnetorheological damper based on Koopman operators. Control Theory Appl 2026;43(1):117–28.
[42] Guo J, Ma C, Yu S, et al. Output feedback H_∞/GH_2 control for in-wheel motor driven semi-active suspensions with nonlinear constraints. J Vib Control 2025. https://doi.org/10.1177/10775463251366710.